technical note technical note

Ice Accretion on a NACA 23012 Airfoil

Ezgi S. Oztekin
Senior Research Scientist, Aircraft Icing Research Program, William J. Hughes Technical Center, NJ 08405

James T. Riley
Program Manager, Aircraft Icing Research Program, William J. Hughes Technical Center, NJ 08405

February 2019

DOT/FAA/TC-TN18/35

U.S. Department of Transportation
Federal Aviation Administration

NOTICE

Technical Report Documentation Page

1. Report No.	2. Government Accession No.	3. Recipient's Catalog No.
DOT/FAA/TC-TN18/35		

4. Title and Subtitle	5. Report Date
Ice Accretion on a NACA 23012 Airfoil	February 2019
	6. Performing Organization Code

7. Author(s)	8. Performing Organization Report No.
Ezgi S. Oztekin[1] James T. Riley[2]	

9. Performing Organization Name and Address	10. Work Unit No. (TRAIS)
[1]Diakon Solutions, LLC, 110 W Beaver Dr, Cape May Court House, NJ 08210 [2]Federal Aviation Administration, William J. Hughes Technical Center, Atlantic City International Airport, NJ 08405	11. Contract or Grant No.

12. Sponsoring Agency Name and Address	13. Type of Report and Period Covered
U.S. Department of Transportation FAA Northwest Mountain Regional Office 1601 Lind Ave SW Renton, WA 98057	14. Sponsoring Agency Code ANM-112

15. Supplementary Notes

The FAA William J. Hughes Technical Center Aviation Research Division COR was Timothy G. Smith.

16. Abstract

A two-part numerical analysis was conducted for a single-element NACA 23012 airfoil. In the first part, Reynolds Averaged Navier Stokes simulations were performed to examine the effect of ice-contamination on aerodynamic performance. The ice-contaminated airfoil geometries were taken directly from icing test campaigns that took place in the NASA Glenn Icing Research Tunnel as part of the SUNSET I project. Lift, drag, and surface-pressure distributions were calculated and compared with the available test data for a range of angles of attack at two model sizes corresponding to low and high Reynolds number flow regimes. It was concluded that two-dimensional steady-state numerical simulations are successful for angles of attack in the pre-stall region, but that they fail near stall angle. In the second part, ice-accretion predictions at conditions selected for the Federal Aviation Regulations 25 Appendix C atmospheric icing conditions were carried out by coupling an external flow solver (NASA OVERFLOW, version 2.2l) with an ice-accretion code (NASA LEWICE2D, version 3.2.2). Comparisons of predicted ice shapes with available ice tracings were made. Chord-wise variation of pressure coefficients was analyzed with and without ice accretion for angles of attack of 2 and 5 degrees at a freestream Mach number of 0.3 and at Reynolds numbers of 3 million and 12 million. For dry-ice cases, accretion predictions were in excellent agreement with the ice tracings. For wet-ice cases, the rate of ice accretion was predicted to be much lower than that for the experimental data.

17. Key Words	18. Distribution Statement
Aircraft ice accretion, Numerical modeling of ice growth, LEWICE2D, Aerodynamic performance degradation of ice contaminated airfoils, Aircraft icing, Icing simulation, Icing modeling.	This document is available to the U.S. public through the National Technical Information Service (NTIS), Springfield, Virginia 22161. This document is also available from the Federal Aviation Administration William J. Hughes Technical Center at actlibrary.tc.faa.gov.

19. Security Classif. (of this report)	20. Security Classif. (of this page)	21. No. of Pages	22. Price
Unclassified	Unclassified	31	

ACKNOWLEDGEMENTS

Authors would like to thank Andy Broeren and William Wright of the NASA Glenn Icing Research Branch, Yoram Yadlin of Boeing Research and Technology, and Tim Smith of the FAA Technical Center.

TABLE OF CONTENTS

LIST OF FIGURES

LIST OF TABLES

LIST OF ACRONYMS

IRT	Icing Research Tunnel
LEWICE2D	2-dimensional ice accretion code developed at NASA Glenn
LWC	Liquid water content
NACA	National Advisory Committee for Aeronautics
ONERA	Office National d'Etudes at Recherches Aérospatiales (French National Aerospace Research Centre)
RANS	Reynolds Averaged Navier-Stokes
Re	Reynolds Number

EXECUTIVE SUMMARY

A two-part numerical analysis was conducted for a single-element NACA 23012 airfoil. In the first part, Reynolds Averaged Navier Stokes simulations were performed to examine the effect of ice-contamination on aerodynamic performance. The ice-contaminated airfoil geometries were taken directly from icing test campaigns that took place in the NASA Glenn Icing Research Tunnel as part of SUNSET I project. Lift, drag, and surface pressure distributions were calculated and compared with the available test data for a range of angles of attack at two model sizes corresponding to low and high Reynolds number (Re) flow regimes. It was concluded that two-dimensional steady-state numerical simulations are successful for angles of attack in pre-stall region but fail near stall angle. In the second part, ice-accretion predictions at conditions selected for the Federal Aviation Regulations 25 Appendix C atmospheric icing conditions [2] were carried out by coupling an external flow solver (NASA OVERFLOW, version 2.2l [3]) with an ice-accretion code (NASA LEWICE2D, version 3.2.2 [4]). Comparisons of predicted ice shapes with available ice tracings were made. Chord-wise variation of pressure coefficients was analyzed with and without ice accretion for angles of attack of 2 and 5 degrees at a freestream Mach number of 0.3 and at Reynolds number of 3 million and 12 million. For dry-ice cases, accretion predictions were in excellent agreement with the ice tracings. For wet-ice cases, the rate of ice accretion was predicted to be much lower than that for the experimental data.

INTRODUCTION

When an aircraft passes through a cloud of super-cooled liquid droplets, ice forms on unprotected lifting and control surfaces, leading to aerodynamic performance losses [1]. Only a two-minute exposure to Federal Aviation Regulations 25 Appendix C atmospheric icing conditions [2] can alter the maximum lift coefficient and the stall angle significantly, depending on the variables determining the ice shape [3]. It is important to improve understanding of the ice-accretion process and the types of ice shapes critical to safety margins of aerodynamic performance [4].

The primary objective of the present work is two-fold:

1. To assess current predictive abilities of two-dimensional (2D) state-of-the-art ice-accretion modeling tools
2. To identify range of applicability of 2D steady-state flow solvers when employed to calculate the performance of ice-contaminated airfoils

The National Advisory Committee for Aeronautics (NACA) 23012 airfoil was chosen because of the existing ice-tunnel ice tracing and wind-tunnel data for this geometry, not only at full-scale but also at one-fourth scale of the full-scale model [5]. Icing tests were conducted for a straight-wing configuration (i.e., the application is two-dimensional). For flow solver, NASA OVERFLOW version 2.2l [6], and for ice-growth modeling, NASA LEWICE2D (2-dimentional ice accretion code developed at NASA Lewis) version 3.2.2 [7], were employed.

The rate of ice-growth was investigated for Appendix C atmospheric icing conditions with liquid water content (LWC) of more than 0.5 at -7.5^{o}C, and for LWC of 0.3 at -20^{o}C, corresponding to wet and dry-ice conditions, respectively. The Reynolds numbers (Re) are 2 million and 13 million for quarter-scale and full-scale models, respectively. The Mach number is $\approx$ 0.3 similar to icing tests simulated in this study. The total spray time, 5 to 10 minutes for the quarter-scale model, was increased to 10 to 20 minutes for the full-scale model to have a similar size of ice deposits. Flow physics were studied by analyzing redistribution of wing surface pressure and change in lift and drag coefficients because of ice deposits. The iced geometries were those predicted by numerical modeling and those taken directly from the scanned ice-accretion data during icing campaigns [5, 8, 9]. For the latter, freestream Mach numbers of 0.18 and 0.3 at a range of angles of attack up to 5 degrees were analyzed.

METHODOLOGY

TEST DATA

The experimental data in the present study are taken from the benchmark ice-accretion database developed for a single-element NACA 23012 straight-wing configuration. The database was the main deliverable of a collaborative research project (SUNSET I) of NASA, the Office National d'Etudes at Recherches Aérospatiales (ONERA), the FAA, and the University of Illinois (UIUC), held from 2004 to 2007 [5]. The database includes not only ice-accretion data but also the

associated aerodynamics data for the examination of effects of ice-contamination on performance characteristics.

The icing test campaigns of SUNSET I were conducted in the Icing Research Tunnel (IRT) of the NASA Glenn Research Center to study ice growth on test articles at two scales: a quarter-scale model of the NACA23012 airfoil with a 46 cm (18 in) chord length and a full-scale model of the same airfoil with a 183 cm (72 in) chord length, both with a 184 cm (72.5 in) span extending from floor to ceiling of the tunnel test section. A selection of ice-contaminated quarter-scale and full-scale configurations were then tested aerodynamically in the UIUC subsonic wind tunnel for a Mach number of 0.18 and an Re of 1.8 million [8, 9], and in the pressurized ONERA F1 subsonic wind tunnel for Mach Numbers ranging from 0.10 to 0.28 and Re of 4.5 million to 16 million [5], respectively. The icing conditions for the IRT tests were selected from the FAA, 14 Code of Federal Regulations (CFR) Part 25 Appendix C [2], and consisted of four ice shape categories named in accordance with the flow field and aerodynamic effects [5]. In the present study, we selected only ten of these test conditions, corresponding to horn and streamwise ice categories, hereafter referred to as wet- and dry-ice categories, respectively, at two angles of attack (2 and 5 degrees), as tabulated in table 1.

Table 1. Simulation matrix for ice-accretion, a subset of IRT test matrix [5]

Scale	Run	U (m/s)	α (deg)	LWC (g/m^3)	MVD (μm)	T (^oC)	time (min)	Ice type	IRT case name
quarter	case 1q	90	5.3	0.64	15	-6.2	10	wet	ED0714
	case 2q	90	5	0.30	15	-21.8	5	dry	ED0730
	case 3q	103	2	0.75	15	-6.5	10	wet	ED0761
	case 4q	103	2	0.33	15	-23.1	10	dry	ED0771
	case 5q	103	2	0.75	15.4	-7.5	5	wet	ED0735/ED1978
full	case 1f	90	5	0.64	15	-6.2	10	wet	EG1163
	case 2f	103	5	0.30	15	-20.7	20	dry	EG1124
	case 3f	103	2	0.50	20	-6.4	22.5	wet	EG1113
	case 4f	103	2	0.30	20	-20.7	10	dry	EG1120
	case 5f	90	5	0.85	20	-6.2	11.25	wet	EG1164

MVD = Median volume diameter

Wet-ice cases 5q and 5f were added to the simulation matrix because they were aerodynamically tested and had measurements of chord-wise pressure variation, lift, and drag coefficients in the SUNSET I database [5, 8, 9]. These two cases were analyzed with aerodynamic simulations for a range of pre-stall angles of attack (up to 5 degrees) as summarized in table 2 along with flight conditions. The freestream Mach number for the quarter-scale model is lower ($M_\infty = 0.18$) because of wind-tunnel limitations (the UIUC wind tunnel is capable of speeds up to $M_\infty = 0.20$ [9]). Although icing conditions for ED0735 [5] and ED1978 [9] are the same, the iced geometries for these two cases differ. In the performance evaluation analysis, scanned-ice geometry for ED1978, similar to an earlier numerical study [10], was employed. The ice-accretion geometries for quarter and full-scale model sizes are shown together in figure 1(b).

Table 2. Simulation matrix for aerodynamic evaluation [5, 8, 9]

Scale	Run	M_∞	Reynold's Number (Re) (10^6)	α (deg)	IRT case name
quarter	case 5q	0.18	1.8	0 to 5	ED1978
full	case 5f	0.29	12.9	0 to 5	EG1164

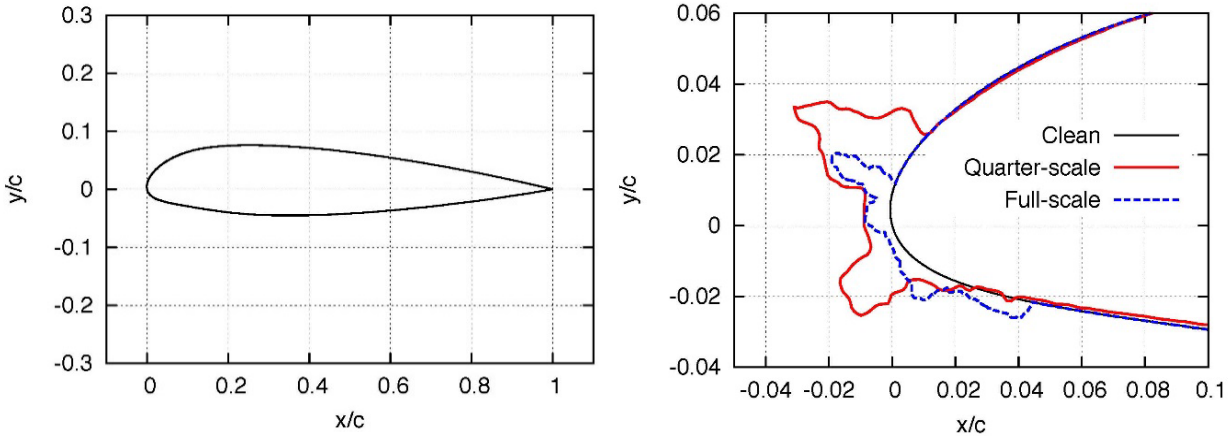

(a) Clean airfoil (NACA23012) (b) Ice-contaminated leading edge

Figure 1. Geometry (non-dimensional): (a) clean airfoil (NACA23012), (b) scanned ice-contaminated geometries at the leading edge for quarter-scale model (ED1978) [9], and full-scale model (EG1164) [5] of SUNSET I database

NUMERICAL MODELING

In this document, two independent numerical analyses on a single-element straight-wing NACA23012 are reported:

1. Aerodynamic performance evaluation
2. Ice-growth modeling

For the aerodynamic performance evaluation, Reynolds Averaged Navier Stokes (RANS) simulations were performed. The first simulation was for a clean airfoil (see figure 1(a)), and another was for an ice-contaminated airfoil at both quarter and full-scale model sizes (see figure 1(b)) in the flight conditions shown in table 2. Chord-wise pressure distributions and change in lift and drag coefficients with varying angles of attack within the pre-stall range were computed and compared with experimental data available in the SUNSET I database for corresponding clean and ice-contaminated airfoils ED1978 and EG1164. For the ice-growth modeling, estimates of ice-accretion were calculated under the icing conditions selected from the SUNSET I database and shown in table 1. The predicted ice shapes were compared with the available ice tracings from icing tunnel experiments for quarter and full-scale model sizes in dry and wet-ice categories.

During the aerodynamic performance analysis, NASA's OVERFLOW solver version 2.2l [6], a general-purpose, implicit computational fluid dynamics (CFD) code that solves Navier-Stokes equations on structured-overset grid systems, was used. In the present study, OVERFLOW was run using the Spalart-Allmaras turbulence model with rotational and curvature correction, the Roe-upwind inviscid-flux algorithm with the Koren flux limiter, and the three-factor diagonal Beam-Warming implicit scheme. For the clean airfoil, the geometry of the model was described with the known coordinates of the NACA23012 airfoil profile [11] shown in figure 1(a). For ice-contaminated airfoil configurations, the ED1978 (quarter-scale) and EG1164 (full-scale) ice-accretion test data shown in figure 1(b) were used. The surface and volume grids for near-body were generated using NASA's Chimera Grid Tools (CGT) [12]. The Cartesian off-body grids were automatically generated through domain connectivity function (DCF) routines in the OVERFLOW-D mode [6]. Integrated forces, lift, and drag were calculated employing the utility program FOMOCO.

In the ice-growth modeling, NASA's ice-accretion solver LEWICE2D version 3.2.2 [7] was employed. The algorithm of LEWICE2D starts with flow-field computations around the surface of interest and calculation of particle trajectories. Once the distribution of liquid water impinging on the surface is determined, local ice-growth rate is computed following the Messinger's thermodynamic model [13]. The growth rate is then multiplied with the specified time increment to predict the ice thickness (i.e., new ice-contaminated geometry). This procedure, initially applied to the clean geometry, is repeated for the newly generated iced geometry until the desired icing time is reached. LEWICE2D has a readily available built-in potential-flow module for flow-field computations, but users were also given the option of inputting flow solutions from outside of LEWICE2D. An external flow solver with LEWICE2D was coupled in an effort to improve the accuracy of ice-accretion predictions. For the external flow solver, OVERFLOW [6] in RANS mode was used. Two-dimensional RANS simulations were performed at each icing time step for all ten cases tabulated in table 1. The icing time step was arbitrarily chosen to be 1 minute in this study (i.e., for a 5-minute icing event, five flow field solutions were needed). For the clean airfoil, the geometry of the model was described with the known coordinates of the NACA23012 airfoil profile [11] shown in figure 1(a). For the new ice-contaminated airfoil for each time step, the updated coordinates of the iced geometry generated in the preceding time step by LEWICE2D was used.

Figure 2 shows 2D grid topology. The computational domain extends -12c to 32c in streamwise (x) direction and -22c to 22c in crosswise (z) direction (figure 2(a)). The grid size of the Cartesian off-body grid at the farfield is 2.5c, which decreases nine levels to 0.005c near the airfoil. The red dashed rectangular area of computational domain in figure 2(a) is zoomed-in to show grid topology close to the airfoil in figure 2(b). A C-type near-body grid with a total number, N_x x N_y, of 279 x 103 is used. As ice grows, the grid structure close to the leading edge changes. A close up view for the clean airfoil and a representative iced-airfoil are provided in figures 2(c) and 2(d), respectively. The ice-contaminated geometry shown is the LEWICE2D solution at 10 minutes into icing for case 1q. Tunnel walls were not modeled in 2D simulations. The total number of grid points is ≈ 0.6 million, significantly lower than would be required for 3D simulations. Freestream, extrapolation, and no-slip boundary conditions were applied at the inflow, outflow, and on solid walls, respectively.

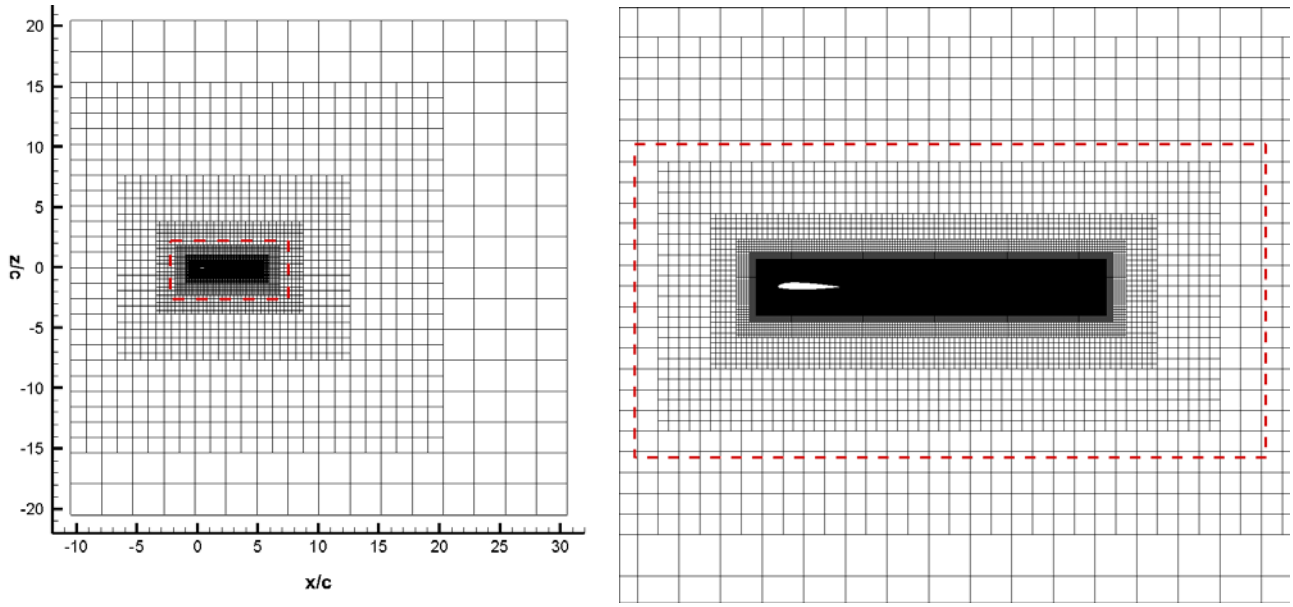

(a) computational domain (b) section of computational domain close to airfoil

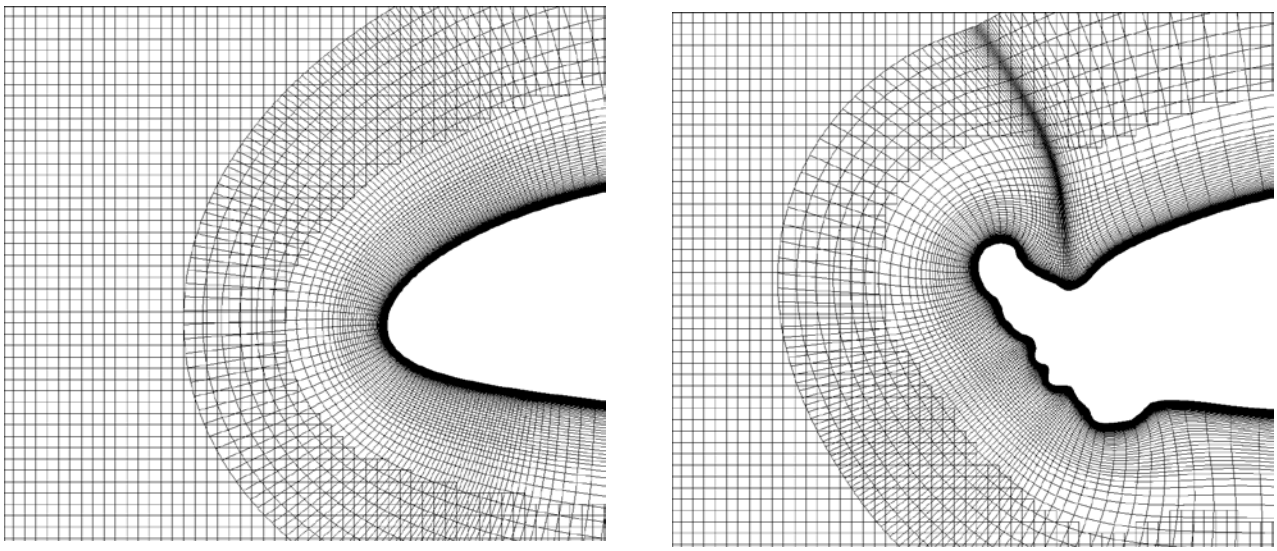

(c) close up for clean airfoil (d) close up for iced airfoil

Figure 2. Grid topology for 2D simulations: (a) computational domain, (b) zoom into the near-body grid, close-up to the leading edge for (c) the clean airfoil, and (d) the representative ice-contaminated airfoil (LEWICE2D run, case1q - 10 minutes into icing)

RESULTS

AERODYNAMIC PERFORMANCE EVALUATION

Simulations were performed for the experimental ice-contaminated airfoil profiles shown in figure 1(b), sweeping angles of attack from 0 to 5 degrees at two model sizes. Figure 3 displays Mach contour plots and streamlines over iced models ED1978 at $\alpha = 2^o$ (first column) and EG1164 at $\alpha = 5^o$ (second column). These configurations are specifically chosen because the ice-accreted geometries were obtained at $\alpha = 2^o$ for ED1978 and at $\alpha = 5^o$ for EG1164. Having clear recirculation regions in the flow field, the effect of ice-contamination is more noticeable for the quarter-scale model (figures 3(a) and 3(c)). Flow separates behind the horns with longer separation regions on the pressure side. It reattach again before 0.15c and smoothly leave the trailing edge. Unlike ED1978, EG1164 is not symmetrical with a taller upper horn because it was obtained at a larger angle of attack ($\alpha = 5^o$). Ice thickness is smaller in comparison to the cross-sectional area for this model size. Because of this, there exists a much shorter recirculation only behind the upper horn (see figures 3(b), 3(d)).

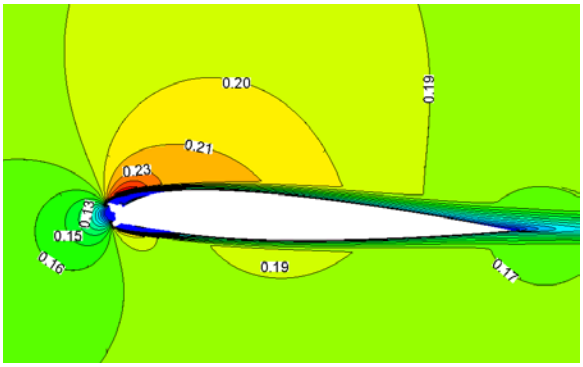

(a) Mach contours for ED1978 at $\alpha = 2^o$

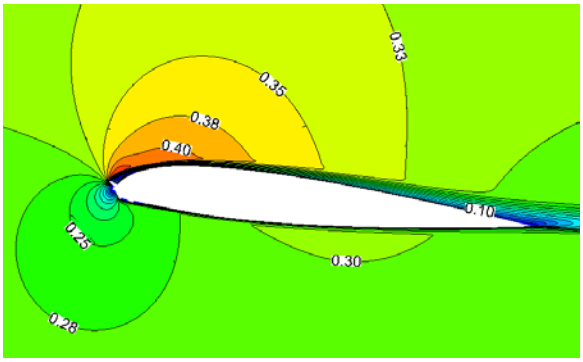

(b) Mach contours for EG1164 at $\alpha = 5^o$

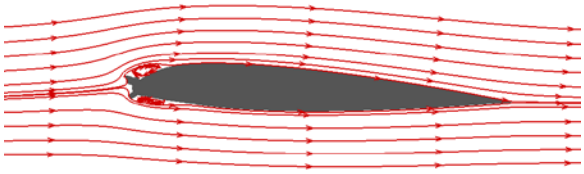

(c) Streamlines for ED1978 at $\alpha = 2^o$

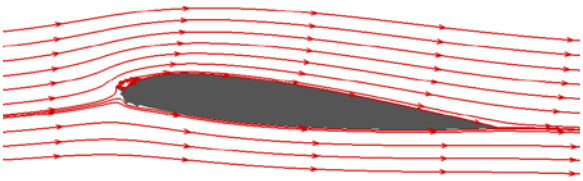

(d) Streamlines for EG1164 at $\alpha = 5^o$

Figure 3. Flow field: (a)(b) Mach contour plots and (c)(d) streamlines over ice-contaminated (a)(c) quarter-scale (ED1978: M_∞=0.18, Re=1.8x10^6) and (b)(d) full-scale (EG1164: M_∞=0.29, Re=12.9 x10^6) models (based on scanned geometries during IRT tests [5, 8, 9])

The full-scale model coefficients of lift, drag, and pressure are calculated at angles of attack of 0, 2, 4, and 5 degrees, and shown along with those obtained during the wind-tunnel tests in figures 4(a), 4(b), and 5, respectively. Measurements indicate that the stall angle decreases with ice-contamination from ≈16 degrees to ≈7 degrees (figure 4(a)). Numerical estimates for the lift coefficient are very close to the measured values for both clean and ice-contaminated airfoils. It changes negligibly between clean and contaminated airfoil in the pre-stall range of angles of attack studied here. There is a noticeable increase in drag coefficient from clean to contaminated airfoil, suggesting that ice deposits has a larger effect on drag coefficient (see figure 4(b)).

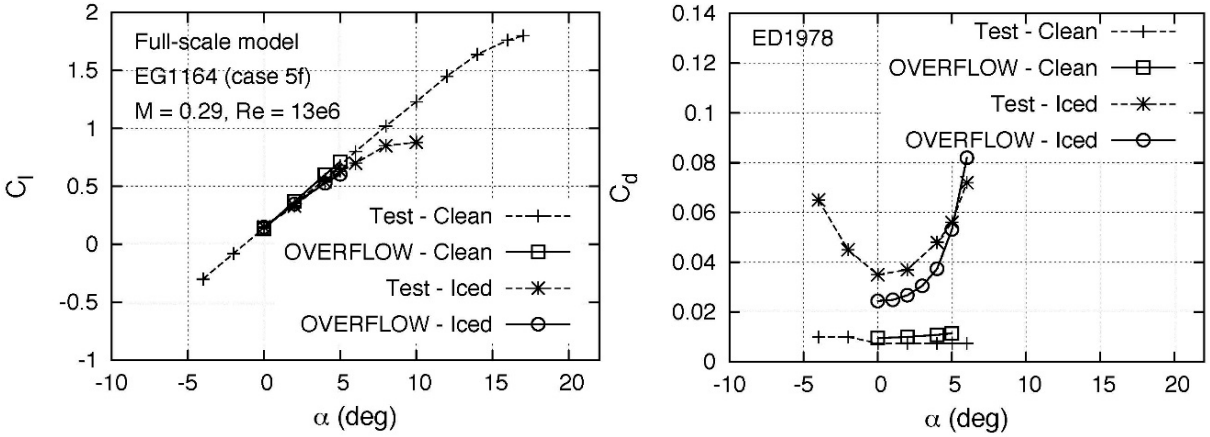

(a) lift coefficient at α = 0, 2, 4, 5° (b) drag coefficient at α = 0, 2, 4, 5°

Figure 4. Full-scale model results: (a) lift and (b) drag coefficients for clean and iced airfoil compared with the test data from the ONERA F1 tunnel [5] (IRT scanned geometries were used [5, 8, 9])

Pressure distributions agree very well with the experimental data for the full-scale model. It is shown in figure 5 at two angles of attacks, α = 0, 4°.

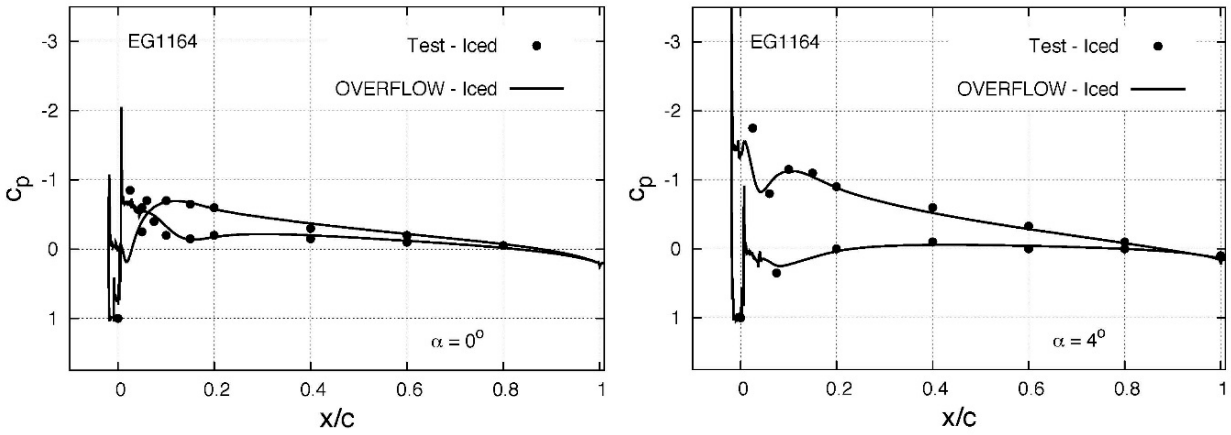

(a) Full-scale, α = 0° (b) Full-scale, α = 4°

Figure 5. Full-scale model results: pressure coefficient for EG1164, M_∞=0.29, Re=12.9x10^6, at (a) α = 0°, and (b) 4° compared with the test data from the ONERA F1 tunnel [5] (IRT scanned geometries were used [5, 8, 9])

Numerical results for the quarter-scale model are not as successful as those for the full-scale ones. Figures 6(a), 6(b), and 7 exhibit, respectively, the predicted lift, drag, and pressure coefficients along with the test data for comparison. Iced geometry simulations were done more often for this model size, with one degree angle increments from α = 0° to 6°. For clean airfoil, simulation results are in agreement with the test data. For ice-contaminated airfoil (ED1978), predictions show an earlier stall (α ≈ 5°) compared to the experimental value of α ≈ 7° (see figure 6(a)). The drag coefficient is considerably under-predicted for the ice-contaminated airfoil at the lower angles of attack studied (see figure 6(b)).

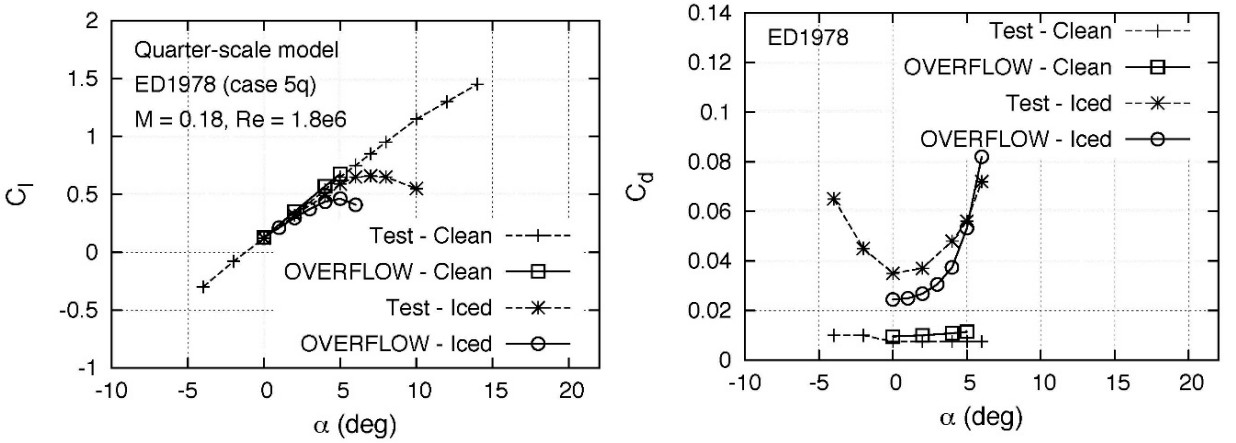

(a) lift coefficient (b) drag coefficient

Figure 6. Quarter-scale model results: (a) lift and (b) drag coefficients for clean and iced airfoil compared with the test data from the UIUC subsonic tunnel [8, 9] (Iced geometry simulations at α = 0° to 6°. IRT scanned geometries were used [5, 8, 9])

The disagreement between experimental data and numerical solution in lift coefficient is observed at angles close to the stall angle. This is also evident from the chord-wise pressure distributions.

Figure 7 displays pressure coefficients along the chord at each angle of attack simulated to identify at what angle the discrepancy in simulation results starts. Surface-pressure predictions are in good agreement with those measured for $\alpha \leq 4^o$, but they are noticeably lower than measured values on the suction side at $\alpha = 5^o$ (see figure 7[f]).

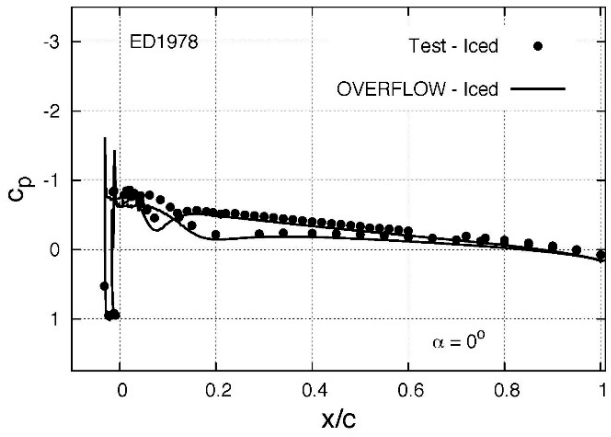

(a) Quarter-scale, $\alpha = 0^o$

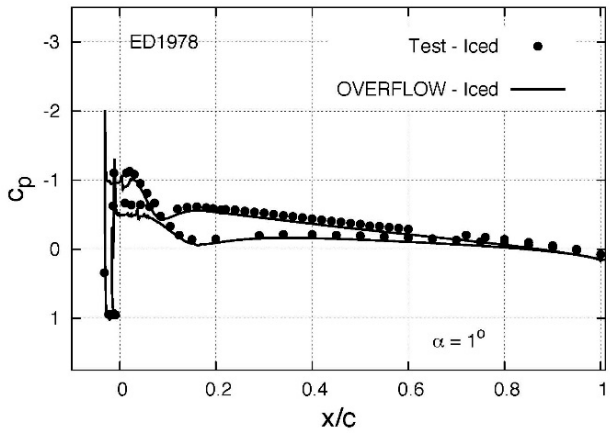

(b) Quarter-scale, $\alpha = 1^o$

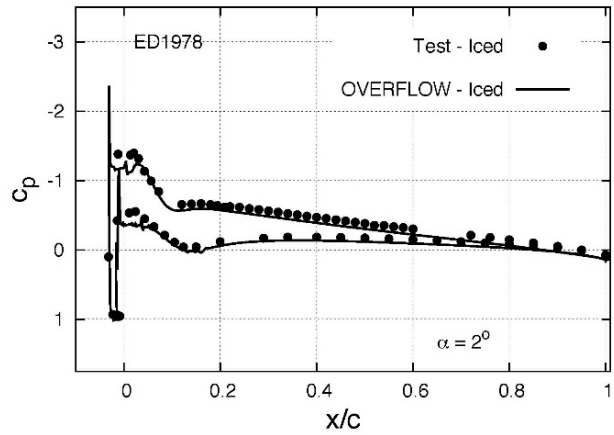

(c) Quarter-scale, $\alpha = 2^o$

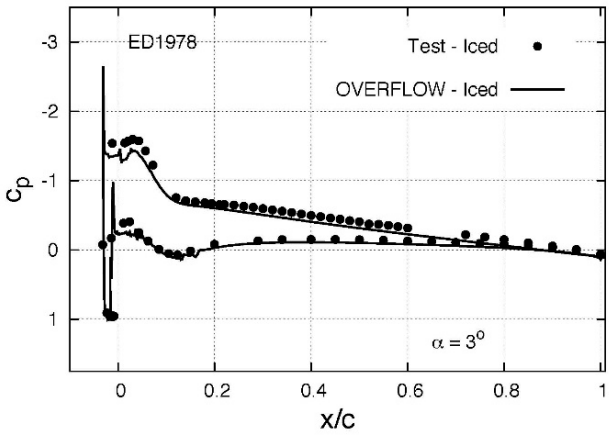

(d) Quarter-scale, $\alpha = 3^o$

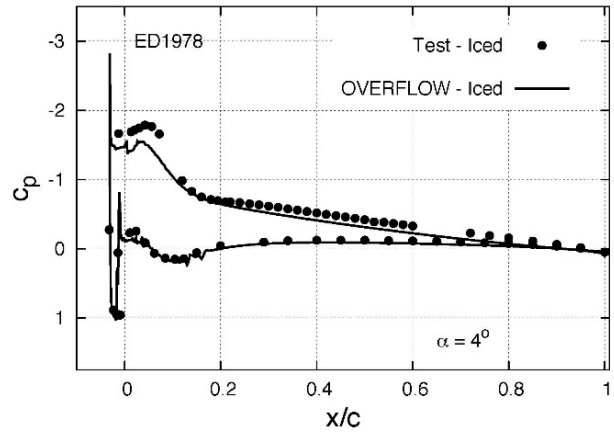

(e) Quarter-scale, $\alpha = 4^o$

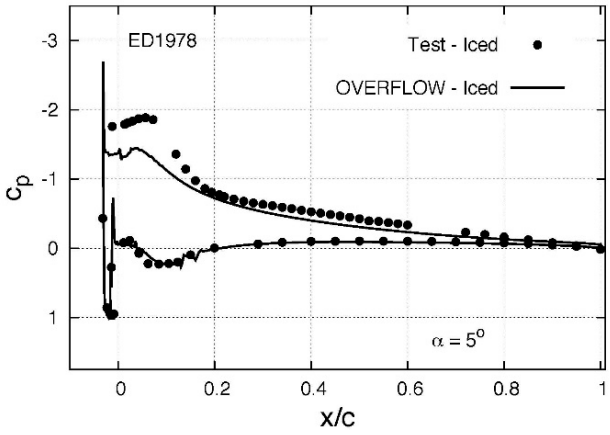

(f) Quarter-scale, $\alpha = 5^o$

Figure 7. Quarter-scale model results: pressure coefficient for ED1978 (M_∞=0.18, Re=1.8x10^6) at (a)-(f) $\alpha = 0^o$ - 5^o compared with the test data from the UIUC subsonic tunnel [8, 9] (IRT scanned geometries were used [5, 8, 9])

Numerical convergence was determined by examining histories of lift and drag coefficients and L2-norm residual, which can be defined as the maximum error obtained as a least-squares sum of residuals calculated at every grid point. For convergence, it is expected to have a drop of at least two to three orders of magnitude in L2-norm. Figures 8(a) and 8(b) display L2-norm residual histories for the full-scale and quarter-scale model sizes, respectively. Solutions of the full-scale model simulations converged to machine precision, as shown in figure 8(a), whereas residuals in the quarter-scale model simulations decreased five orders of magnitude at lower angles of attack, and less than that for $\alpha = 5^o$ and $\alpha = 6^o$. As the angle of attack is increased to $\alpha = 5^o$, convergence behavior changes, and at $\alpha = 6^o$, it deteriorates drastically. This can be seen in figure 8(b).

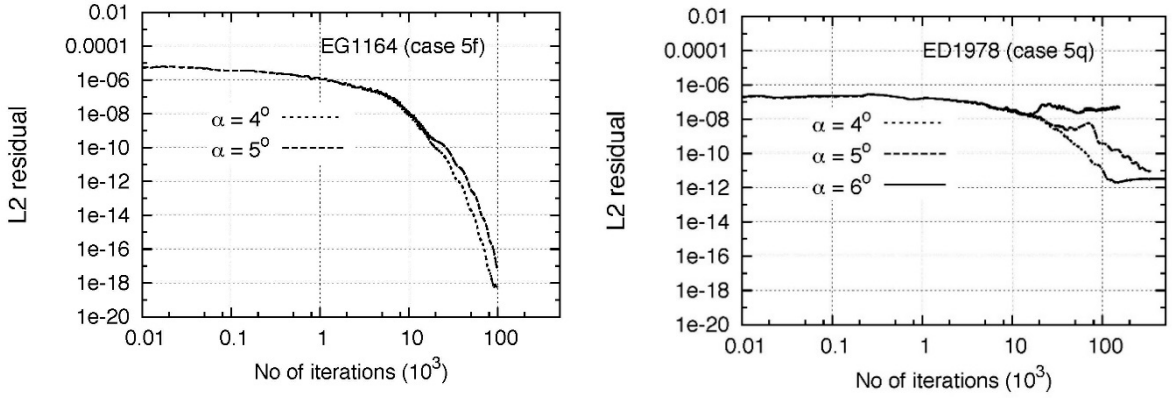

(a) EG1164 (b) ED1978

Figure 8. Convergence history: L2 residual for (a) full-scale and (b) quarter-scale models

The effect of transients is also evident in figure 9, which shows the convergence history of lift and drag coefficients. The large oscillations in lift and drag coefficients for $\alpha = 6^o$ can be clearly seen in figure 9, and indicate that two-dimensional steady-state simulations are not sufficient for angles of attack closer to the stall angle. Because results obtained at lower angles of attack are very similar to those obtained at $\alpha = 4^o$ for both model sizes, they are not shown in the figures.

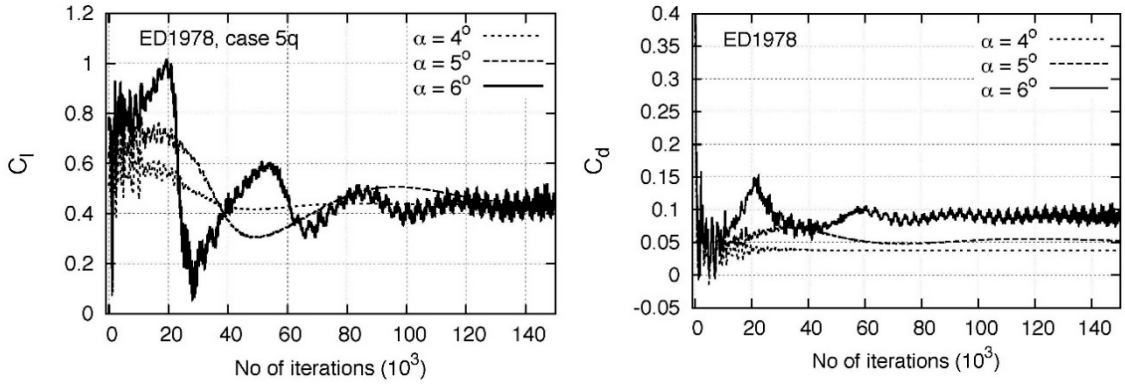

(a) lift coefficient (b) drag coefficient

Figure 9. Convergence history: (a) lift and (b) drag coefficients for quarter-scale model ED1978

ICE-ACCRETION SIMULATIONS

1- Ice-shape comparisons

Simulations for ice-accretion modeling were performed in two dimensions using both the panel method (built-in potential flow solver) available with LEWICE2D and OVERFLOW with the total number of OVERFLOW iterations set to 30,000 for each time step. Convergence was checked by monitoring L2-norm of residuals and drag and lift coefficients. To speed up the convergence rate, simulations were restarted from the solution of the previous time step. In general, drag coefficients converged faster than the lift coefficients. Lift coefficients took longer to converge as the amount of ice deposits increased, most noticeably for the quarter scale wet-ice cases. The results show that ice contamination had a larger influence on drag than on lift characteristics as compared to the clean airfoil.

The simulations are analyzed in three groups: dry-ice cases, wet-ice cases, and time evolution of wet-ice cases. For dry-ice cases, change in aerodynamic performance is minimal at the conditions studied. For wet-ice cases, drag coefficient increased substantially. For the quarter-scale model, drag coefficient increased three fold compared to that of the clean airfoil. These results are consistent with previous experimental work [8]. Figures 10–12 show model predictions using OVERFLOW (red solid lines) and the panel method (blue dashed lines) available with LEWICE2D overlaid on experimental data (black solid lines). Comparisons for dry and wet-ice conditions are displayed in figures 10 and 11 for quarter-scale (first column) and full-scale (second column) cases. Test data include ice tracings at different spanwise locations (typically at 24, 36 and 48 in), and the mid-span tracing (at 36 in), when available, is plotted darker in the figures for reference purposes. In some cases, there are no data at midspan, such as case 3q, shown in figure 11(c). In others, there is more than one dataset available at midspan, such as cases 2q and 3f in figures 10(a) and 11(d), respectively. Both midspan tracings are kept to show uncertainty in the test data, even measured at the same location.

For dry-ice cases (figure 10), model estimates are generally good. The ice thickness and distribution, and the lower and upper impingement limits, are captured well and within experimental uncertainty. OVERFLOW and the panel method yield similar results, except for case 4q of the quarter-scale geometry for which the leading-edge ice is predicted slightly thicker using OVERFLOW (see figure 10(c)).

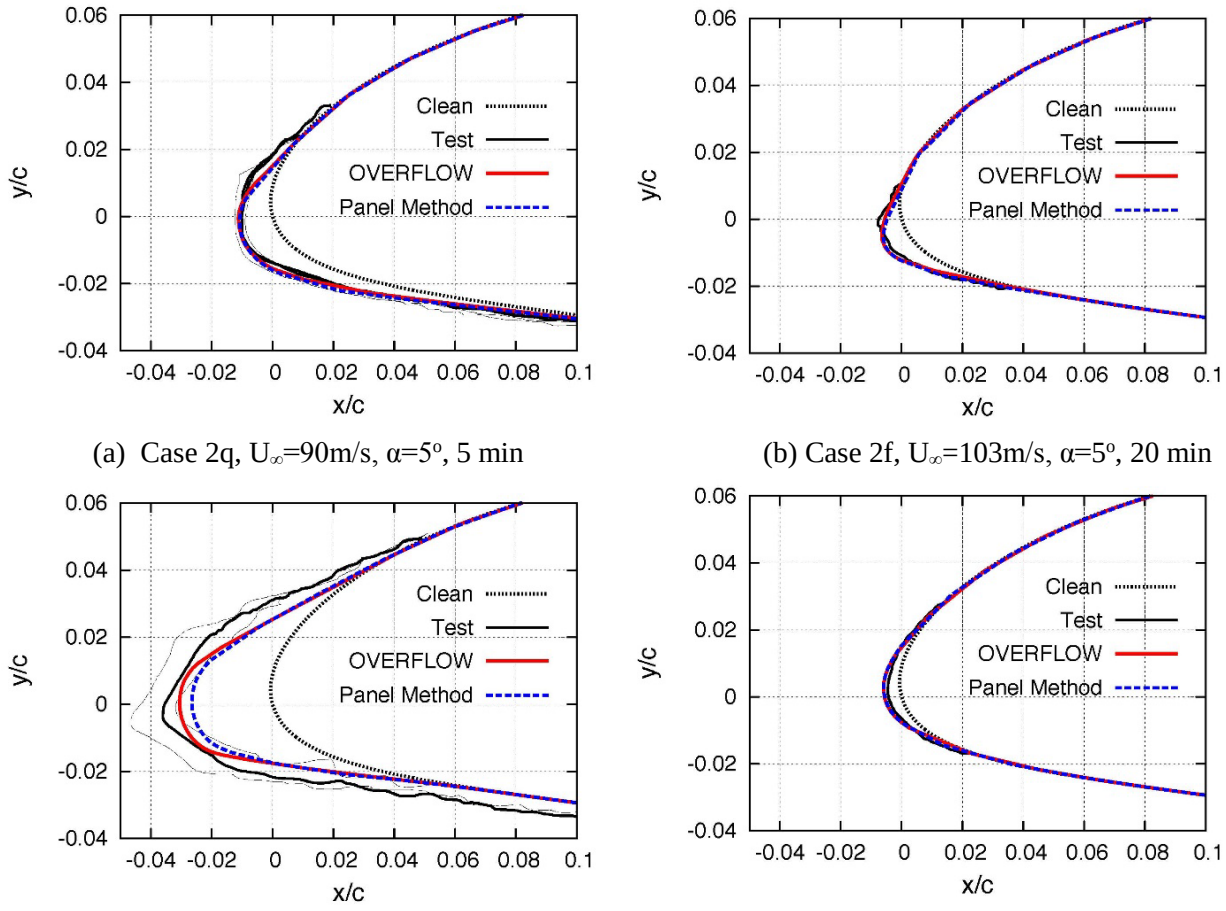

(a) Case 2q, U_∞=90m/s, α=5º, 5 min

(b) Case 2f, U_∞=103m/s, α=5º, 20 min

(c) Case 4q, U_∞=103m/s, α=2º, 10 min

(d) Case 4f, U_∞=103m/s, α=2º, 10 min

Figure 10. Dry-ice cases (T≈-20ºC): comparisons between test data and predictions for (a)(c) the quarter-scale and (b)(d) the full-scale models (See table 1 for test conditions of each case)

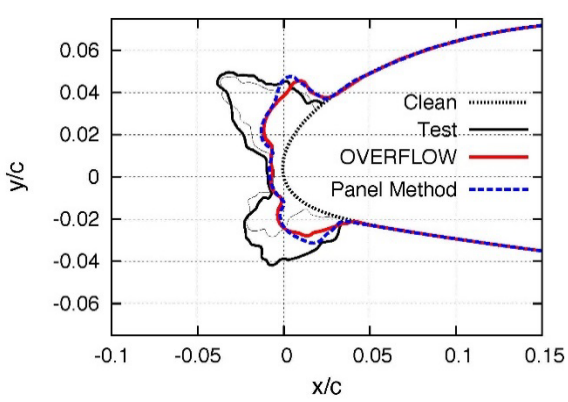

(a) Case 1q, U_∞=90m/s, α=5°, 10 min

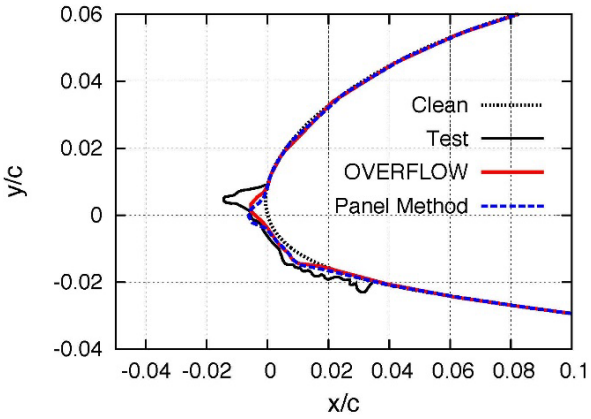

(b) Case 1f, U_∞=90m/s, α=5°, 10 min

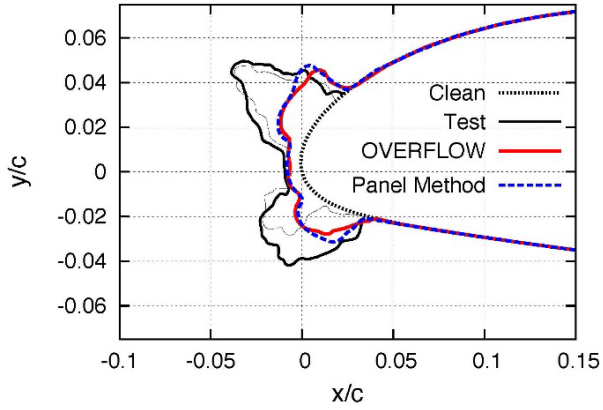

(c) Case 3q, U_∞=103m/s, α=2°, 10 min

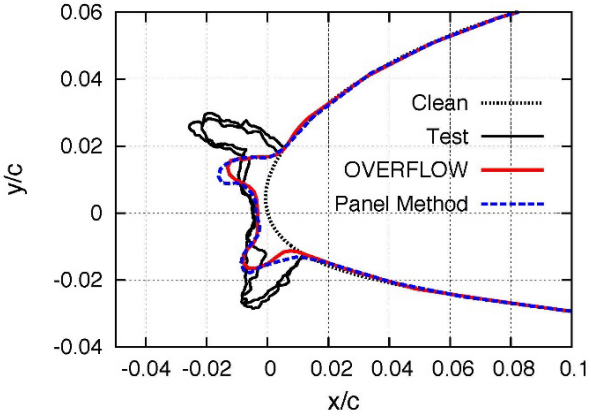

(d) Case 3f, U_∞=103m/s, α=2°, 23 min

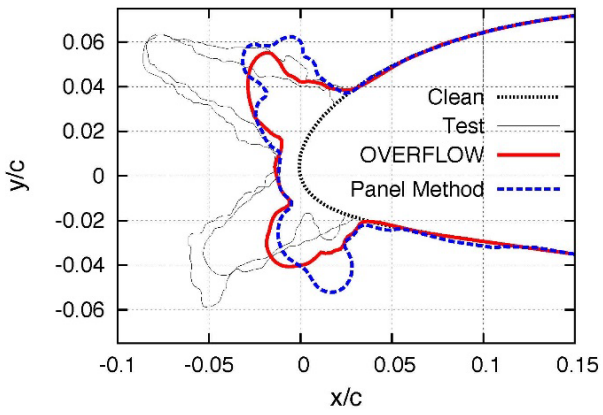

(e) Case 5q, U_∞=103m/s, α=2°, 5 min

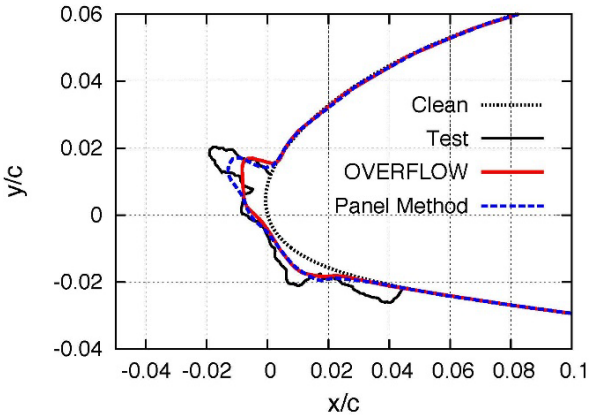

(f) Case 5f, U_∞=90m/s, α=5°, 11 min

Figure 11. Wet-ice cases (T≈-7.5° C): comparisons between test data and predictions for (a)(c)(e) the quarter-scale and (b)(d)(f) the full-scale models (See table 1 for test conditions of each case)

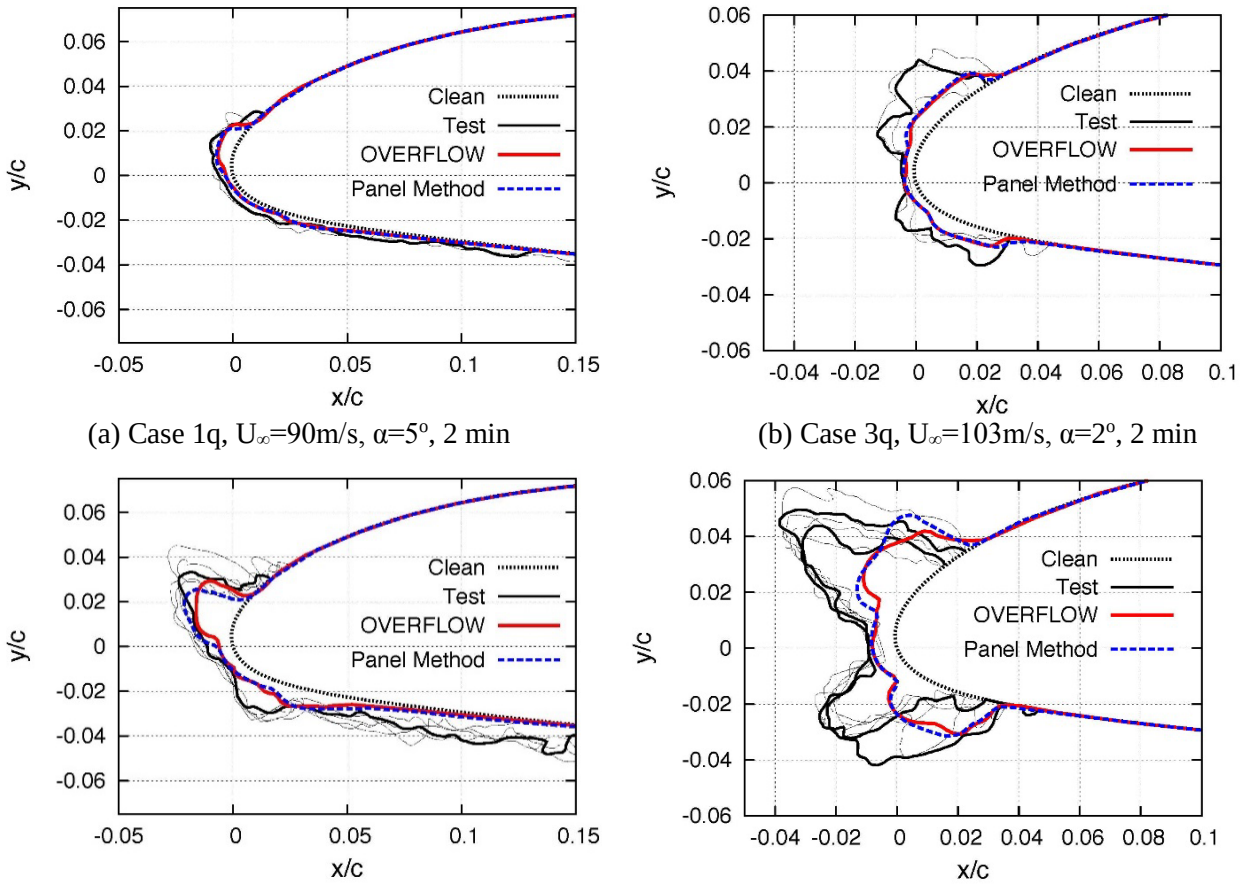

(a) Case 1q, U_∞=90m/s, α=5º, 2 min

(b) Case 3q, U_∞=103m/s, α=2º, 2 min

(c) Case 1q, U_∞=90m/s, α=5º, 5 min

(d) Case 3q, U_∞=103m/s, α=2º, 5 min

Figure 12. Wet-ice cases (T≈-7.5º C): time evolution comparisons between test data and predictions for case 1q (first column) and case 3q (second column) quarter-scale model at (a)(b) two-min and (c)(d) five-min into icing

For wet-ice cases (figure 11), predictions are not as successful, and there exist noticeable differences between OVERFLOW and panel method solutions. For case 1q, shown in figures 11(a) and 11(b), model estimates for the horn heights and the lower impingement length are smaller in comparison to the test data. For case 3q, though the footprint is well-predicted, the total amount of ice mass is grossly underestimated for both quarter-scale and full-scale geometries (see figures 11(c) and 11(d)). Similar results are found for case 5q. For quarter-scale geometry, having similar test conditions for case 3q, results reveal deviations from the test data much earlier, at 5 minutes into the icing event.

Time evolutions of ice accumulation are examined in figure 12 for quarter-scale model case 1q (first column) and case 3q (second column). This is made possible using icing tunnel experiments at identical tunnel conditions for times of 2 minutes and 5 minutes. For case 1q, the discrepancy in lower impingement limit estimation is much more marked for 5 minutes than 2 minutes of icing (figure 12(c)), whereas for case 3q, the under-prediction of added-ice mass can be seen as early as 2 minutes into icing (figure 12(b)). The disagreement between predictions and test data is more readily noticeable for lower angle of attack cases (case 3q) because asymmetry tends to divert

attention to the upper surface and away from runback effects on the lower surface as the angle of attack increases (case 1q).

All simulations were carried out using the built-in heat-transfer-coefficient correlations of LEWICE2D, except for quarter-scale case 1q. Simulations for this case were first conducted with the LEWICE2D correlations, then repeated using heat-transfer-coefficients calculated from the OVERFLOW solution (shown in red-dotted lines in figure 13(b) as OVERFLOWhtc). These calculations did not include roughness effects, resulting in a decrease in heat-transfer-coefficient values in comparison to that of LEWICE2D. Figure 13(a) exhibits comparisons of the heat-transfer coefficient values after the first time-step. For case 1q, using computed heat-transfer coefficients instead of built-in correlations altered the upper- and lower-horn shape but not the total added-ice amount. LEWICE2D in its current formulation employed in this study follows the Messinger model in its original form and assumes that heat conduction is negligible compared to convection if there is no thermal ice protection. Myers [14] suggested that neglecting conduction terms may result in underestimation of added ice amount for wet-ice conditions. In a separate study, Bourgault et al. [15] also found conductive heat fluxes to be crucial in their application of water surface runback formulations.

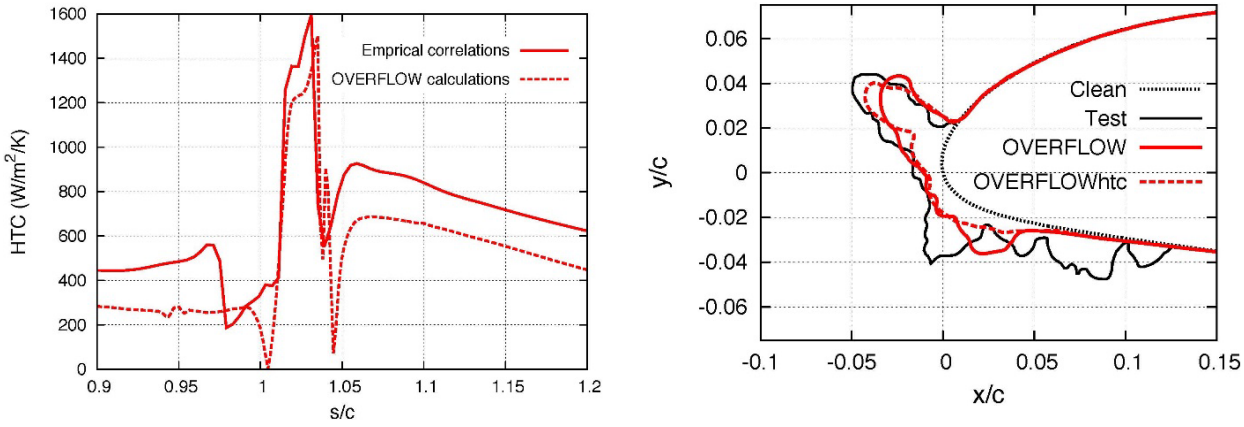

(a) Heat transfer coefficient

(b) Ice shape comparisons

Figure 13. Comparisons between (a) heat transfer coefficients calculated from correlations, and OVERFLOW and (b) corresponding ice-shape predictions

2- Flow-field comparisons for numerically predicted ice shapes

The most severe dry and wet-ice cases, those with the maximum spray time (table 1), are chosen to examine the influence of leading-edge ice on flow physics. These are cases 4q and 1q at quarter-scale model sizes, and cases 2f and 3f at full-scale model sizes, tested respectively under dry and wet-ice conditions. Mach number contours in figure 14, streamlines in figure 15, and pressure coefficient in figure 16 display the level of flow disturbance depending on the relative size and shape of ice contamination. For dry-ice cases, the airfoil nose protrudes into the incoming stream with a smooth transition following the clean airfoil contours in a way that makes it difficult to distinguish where deposits starts (see figures 14(a), 14(b), 15(a), and 15(b)). These cases show negligible effects on the flow field, whereas for wet-ice cases there is a distinct profile change with

additional horn-like protrusions grown normal to the airfoil surface (see figures 14(c), 14(d), 15(c), and 15(d)). Depending on their relative size, flow physics may change drastically.

The upper horn for the quarter-scale wet-ice case is the largest protuberance, having a height close to 0.06c, and results in flow separation, as shown in figures 14(c) and 15(c). Flow reattaches behind the horn but separates again close to the trailing edge. The vortices behind the horns and at the trailing edge can be clearly seen in figure 15(c). For case 2f, shown in figure 14(b), Mach contours on the suction side are much higher than those for case 1q, shown in figure 14(c) at the same angle of attack. Though case 2f is a dry-ice case, the deposits is so small that the flow physics is similar to that for the clean airfoil.

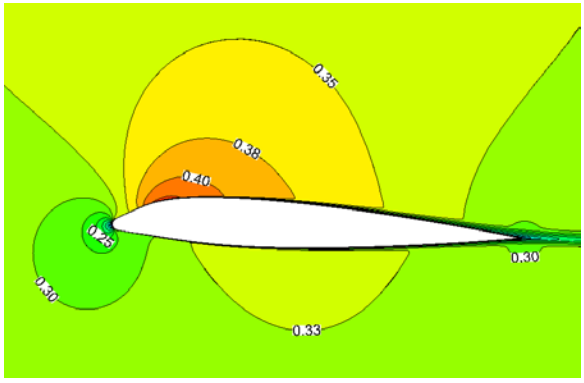

(a) Dry-ice: case 4q, U_∞=103m/s, α=2º, 10 min

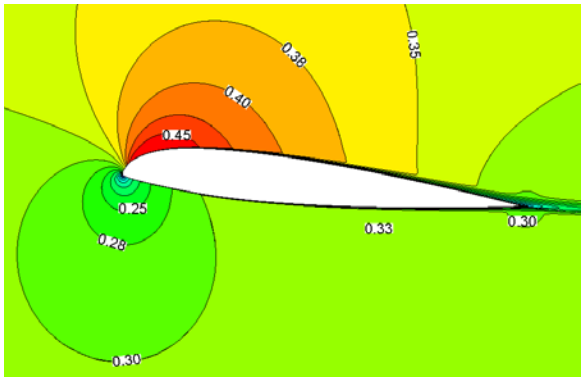

(b) Dry-ice: case 2f, U_∞=103m/s, α=5º, 20 min

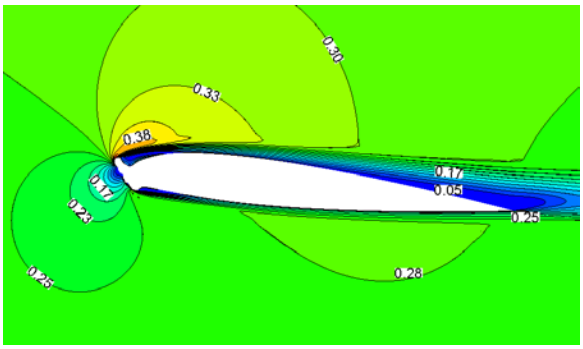

(c) Wet-ice: case 1q, U_∞=90m/s, α=5.3º, 10 min

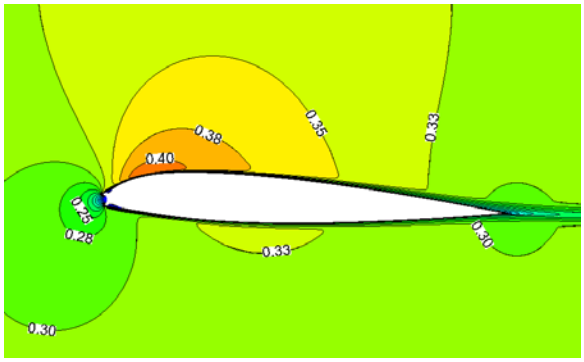

(d) Wet-ice: case 3f, U_∞=103m/s, α=2º, 23 min

Figure 14. Mach contour plots over ice-contaminated airfoils for: (a)(b) dry-ice (T ≈ -20º C) (first row), (c)(d) wet-ice (T ≈ -7.5º C) (second row), (a)(c) quarter-scale (first column), and (b)(d) full-scale (second column) cases (Iced geometries were predicted by LEWICE2D)

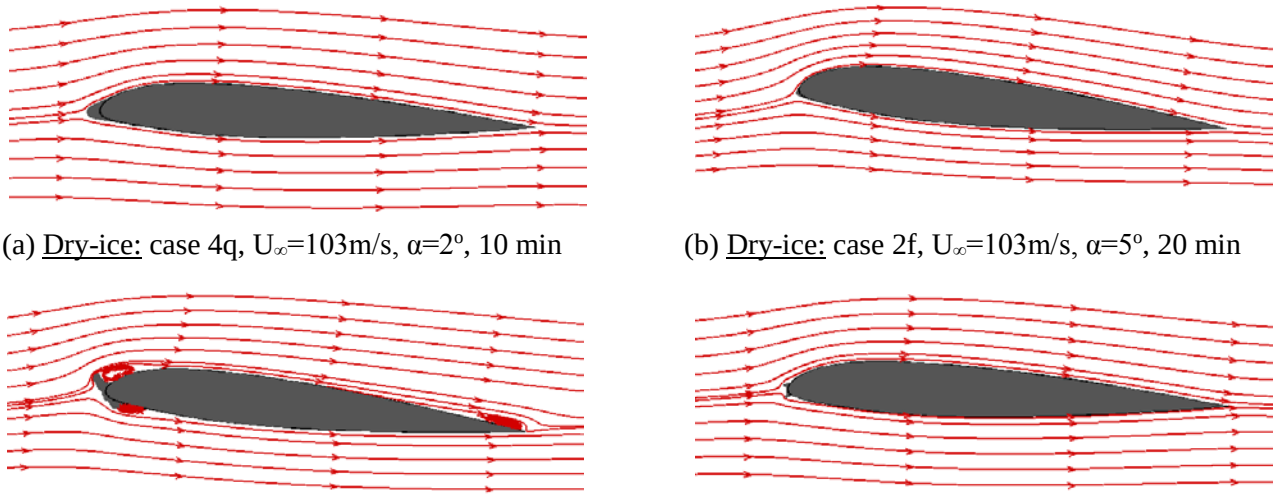

(a) Dry-ice: case 4q, U_∞=103m/s, α=2º, 10 min

(b) Dry-ice: case 2f, U_∞=103m/s, α=5º, 20 min

(c) Wet-ice: case 1q, U_∞=90m/s, α=5.3º, 10 min

(d) Wet-ice: case 3f, U_∞=103m/s, α=2º, 23 min

Figure 15. Streamlines over ice-contaminated airfoils for: (a)(b) dry-ice (T ≈ -20º C) (first row), (c)(d) wet-ice (T ≈ -7.5º C) (second row), (a)(c) quarter-scale (first column), and (b)(d) full-scale (second column) cases (Iced geometries were predicted by LEWICE2D)

At full-scale model size, the amount of ice deposits is negligibly small in comparison to the airfoil cross-sectional area not only under dry-ice conditions (see figures 14(b) and 15(b)), but also under wet-ice conditions, even at 23-minutes into icing (see figures 14(d) and 15(d)). It is remarkable to see almost identical Mach contour plots for the dry-ice case at quarter-scale (case 4q) in figure 14(a), and those for the wet-ice case at full-scale (case 3f) in figure 14(d). Though the shape of deposits are different for these two cases, the flow disturbances are similarly insignificant, as seen in figures 15(a) and 15(d). The inflow Mach number for these runs were determined using the free-stream conditions listed in table 1, which is the same regardless of model size. Because results are not compared with the experimental data for the iced-geometry, there is no limitation on the free-stream velocity that would have been otherwise set by the size of the wind tunnel.

Chord-wise surface pressure distributions were calculated for the ice-contaminated airfoils and compared with those of the clean airfoils for the same selected set of quarter-scale (shown in the first column) and full-scale (shown in the second column) cases, along with the experimental data for the clean airfoil in figure 16. Pressure test data are not available for iced geometries. In general, predictions for clean airfoil agree well with the experimental data. For dry-ice conditions, the effect of ice contamination is minimal, especially for the full-scale airfoil case (figure 16(b)). For wet-ice conditions, a pressure peak is observed on both suction and pressure sides of the contaminated airfoils (figures 16(c) and 16(d)). For the quarter-scale wet-ice case, pressure drops after the initial peak on the suction side. For the full-scale wet-ice case, there is not much change in the pressure field, except for a small region close to the leading edge. The lift coefficient for case 1q is calculated to be ≈0.5, that for the clean airfoil at the same configuration is computed to be ≈0.7, indicating more than 20% deterioration in lift. The stagnation point moves forward because of ice deposits, particularly noticeable in the quarter-scale cases shown in figures 16(a) and 16(c).

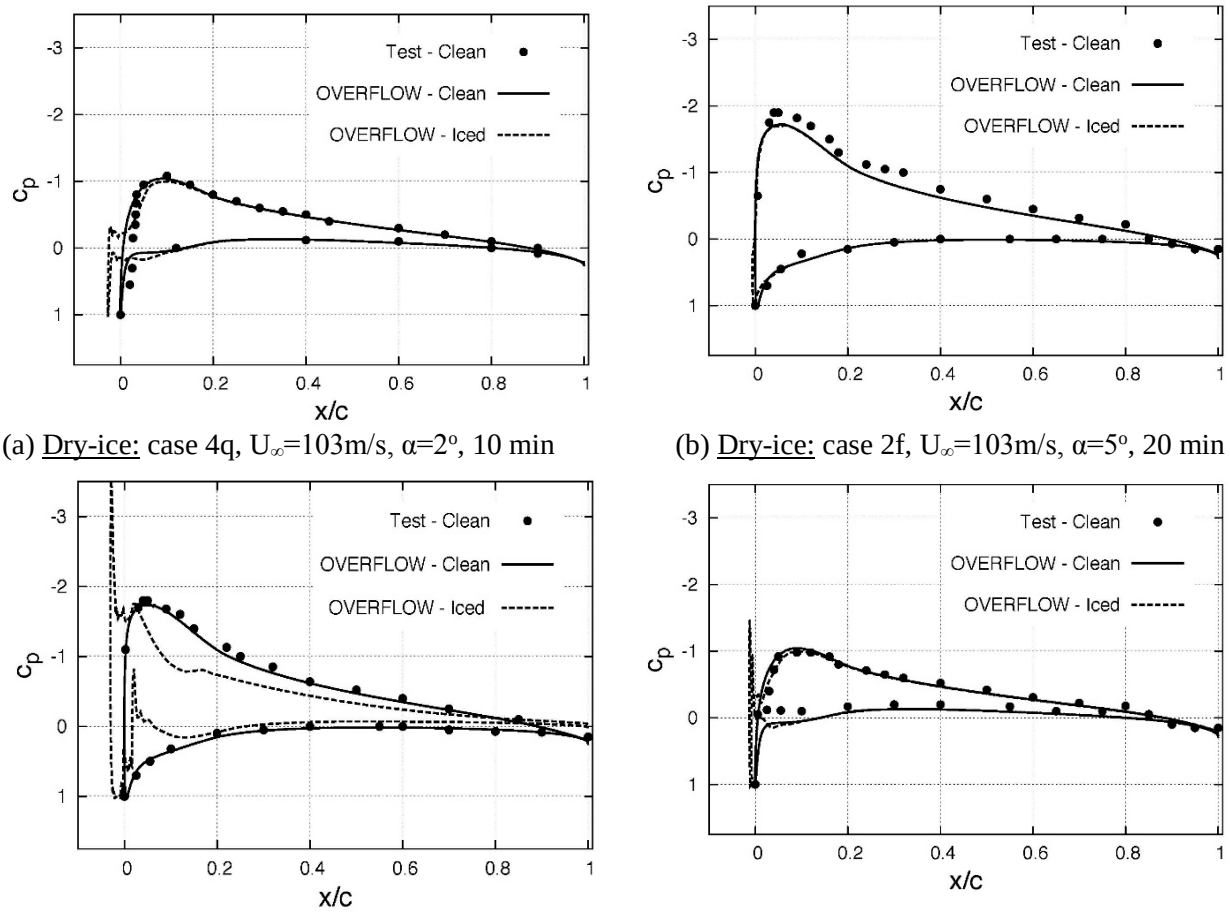

(a) Dry-ice: case 4q, U_∞=103m/s, α=2º, 10 min

(b) Dry-ice: case 2f, U_∞=103m/s, α=5º, 20 min

(c) Wet-ice: case 1q, U_∞=90m/s, α=5.3º, 10 min

(d) Wet-ice: case 3f, U_∞=103m/s, α=2º, 23 min

Figure 16. Pressure coefficient: comparisons of clean and ice-contaminated airfoils for selected (a)(b) dry-ice (T ≈ -20º C) (first row), (c)(d) wet-ice (T ≈ -7.5º C) (second row), (a)(c) quarter-scale (first column), and (b)(d) full-scale (second column) cases (Iced geometries were predicted by LEWICE2D)

CONCLUSIONS

Ice accretion on a NACA23012 straight-wing configuration is numerically investigated, first by simulating the aerodynamic performance of experimental ice shapes obtained in Icing Research Tunnel (IRT) test campaigns [5, 8, 9], and second by modeling the ice-accretion process itself starting from a clean airfoil configuration. In the first study, two geometries, one at full-scale and another at quarter-scale model sizes, were analyzed to evaluate performance losses because of ice-contamination. For this purpose, iced geometries EG1164 for full-scale and ED1978 for quarter-scale model sizes, generated under wet-ice conditions in IRT test campaigns [5] and later tested aerodynamically in wind-tunnel campaigns [5, 8, 9], were chosen because they have performance data and ice tracings. RANS simulations were conducted at a Mach number of 0.18 and Re of 2 million for quarter-scale model, and at a Mach number of 0.29 and Re of 13 million for full-scale model at angles of attack of 0 to 5 degrees. Comparisons were made between simulation results and the available test data, and the range of applicability of two-dimensional steady-state RANS

simulations was investigated. It was concluded that two-dimensional steady-state RANS simulations are successful in the pre-stall region but fail as stall angle is approached.

In the second study, an external flow solver was coupled with an ice-accretion modeling tool in a time-stepping algorithm to estimate ice deposits on full-scale and quarter-scale airfoil models. A larger set of test cases under various icing conditions, ranging from dry to wet ice, were analyzed. The flow field and the heat-transfer coefficient obtained from the external flow solver was read into the ice-accretion code to examine the effect of heat-transfer calculations. However, these calculations were limited as they did not include surface roughness effects. Comparisons of predicted ice shapes with available ice tracings were made, and aerodynamic performance losses were numerically examined. Regardless of the model size, ice-accretion simulation results showed excellent comparisons with the available experimental data under dry-ice conditions, but failed to accurately predict the added-ice amount under wet-ice conditions. This may indicate the significance of runback and heat-transfer formulations in ice-accretion modeling. The effect of ice-contamination on aerodynamic performance was found to be negligible for all dry-ice cases and for all full-scale model cases studied, but entailed a significant performance degradation for the quarter-scale model under wet-ice conditions.

REFERENCES

1. NASA Report. (2007). Papadakis, M., Wong, S.-C., Rachman, A., Hung, K. E., Vu, G. T., and Bidwell, C. S., Large and Small Droplet Impingement Data on Airfoils and Two Simulated Ice Shapes. (NASA TM-2007-213959).

2. Appendix C to Part 25, Atmospheric Icing Conditions. 14 CFR Appendix C to Part 25, sub-chapter C - Aircraft, Part 25 – Airworthiness Standards: Transport Category Airplanes, (2009).

3. NASA Report. (2000). Ice Accretions and Icing Effects for Modern Airfoils. (NASA TP-2000-210031).

4. Bragg, M. B., Broeren, A. P., and Blumenthal, L. A. (2005). Iced-airfoil aerodynamics. Progress in Aerospace Sciences, 41(5), 323–362.

5. NASA Report. (2016). Ice Accretions and Full-Scale Iced Aerodynamic Performance Data for a Two-Dimensional NACA 23012 Airfoil. (NASA/TP-2016-218348).

6. Nichols, R. H. and Buning, P. G., “NASA Report. (2016). User's Manual for OVERFLOW Version 2.2.," Tech. rep., NASA, Feb. 2016, https://overflow.larc.nasa.gov/home/users-manual-for-overflow-2-2/ [retrieved 2016].

7. NASA Report. (2008). User Manual for the NASA Glenn Ice Accretion Code LEWICE Version 3.2.2. (NASA CR-2008-214255).

8. NASA Report. (2011). Aerodynamic Simulation of Ice Accretion on Airfoils. (NASA TP-2011-216929).

9. NASA Report. (2015). Validation of 3-D Ice Accretion Measurement Methodology for Experimental Aerodynamic Simulation. (NASA TP-2015-218724).

10. König, B., Fares, E., and Broeren, A. P. SAE Report. (2015). Lattice-Boltzmann Analysis of Three-Dimensional Ice Shapes on a NACA 23012 Airfoil. (2015-01-2084).

11. Airfoil Tools. (n.d.). http://airfoiltools.com/airfoil/details?airfoil=naca23012-il [retrieved 2016].

12. Chan, W. M., Rogers, S. E., Panda, S. A., Kao, D. L., Buning, P. G., Meakin, R. L., Boger, D. A., and Nash, S. M. (2010). "Chimera Grid Tools User's Manual, Ver. 2.1", NASA, March 2010, http://people.nas.nasa.gov/wchan/cgt/doc/man.html [retrieved 2014].

13. Messinger, B. (1953). Equilibrium Temperature of an Unheated Icing Surface as a Function of Air Speed. *Journal of Aeronautical Sciences*, *20*(1), 29–42.

14. Myers, T. G. (2001). Extension to the Messinger Model for Aircraft Icing. *AIAA Journal*, *39*(2), 211–218.

15. Bourgault, Y., Beaugendre, H., and Habashi, W. G. (2000). Development of a Shallow-Water Icing Model in FENSAP-ICE. *Journal of Aircraft*, *37*(4), 640–646.